Earth and Space Science

Key Points:

- A fiber optic embedded within a legacy energy cable is interrogated using distributed sensing techniques for 12 hr
- The cable strain data captures the modulation of near-coast wave breaking by tidal changes in water depth
- Strain is shown to be linearly related to the local velocity, highlighting the potential for high space-time resolved velocity sensing

Correspondence to:
C. P. Spingys,
carl.spingys@noc.ac.uk

Distributed Optical Fibre Sensing for High Space-Time Resolution Ocean Velocity Observations: A Case Study From a Macrotidal Channel

Carl P. Spingys[1] , **Alberto C. Naveira Garabato[2]** , **and Mohammad Belal[1,3,4]**

[1]National Oceanography Centre, Southampton, UK, [2]Ocean and Earth Science, University of Southampton, Southampton, UK, [3]Department of Mathematical Sciences, University of Liverpool, Liverpool, UK, [4]Department of Physics, University of Southampton, Southampton, UK

Abstract Despite significant recent technological advances, oceanographic observations on horizontal scales of meters to a few kilometres prove challenging. Exploiting legacy seafloor cables presents a disruptive prospect to address this gap, as it may provide low-cost sustained observations with high space-time resolution, enabled through novel opto-electronic interrogation of optical fibers within the cables. Here, we demonstrate this approach in a renewable tidal energy cable embedded within a region with a strong barotropic tide. By making remote measurements continuously over 12 hr, we obtain the distributed differential strain experienced by 2 km of offshore cable from a diverse range of oceanic flow processes, with an along-cable resolution of 2.04 m. We successfully identify: (a) nearshore wave breaking and its modulation by changes in water depth; (b) along-cable tidal velocity, shown to be linearly related to the differential strain; and (c) high-frequency motions consistent with 3-dimensional turbulent processes, either of natural origin or from flow-cable interaction. These inferences are supported by nearby conventional measurements of water depth and velocity.

Plain Language Summary While new marine observational tools have greatly improved our understanding of the oceans, a gap in our ability to observe processes occurring on scales of meters to a few kilometers still persists. In this study, we demonstrate the use of a legacy seafloor cable as a disruptive observational platform to enable oceanic velocity measurements on such scales. Using this cable, we measure: (a) surface wave breaking at the beach; (b) the along-cable water-velocity from the stretching and compression of the cable; and (c) fast motions associated with small-scale ocean turbulence. These observations are supported by conventional oceanographic measurements in the same region. Our results highlight the potential of legacy seafloor cabled infrastructure, comprising both energy and telecommunications cables, for sustainably obtaining high-resolution observations of ocean circulation at low cost.

1. Introduction

Decades of technological advances in ocean observation (Davis et al., 2019) have made it possible to measure oceanic phenomena across a wide range of spatio-temporal scales and extents, from the O(1 cm, 1 s) of three-dimensional turbulence to the O(1,000–10,000 km, 1–10 years) of climatic variations in basin-wide over-turning. This richness of observations has been instrumental in driving physical oceanography toward a state of maturity—in which characterization of the ocean's operation and climatic role is beginning to routinely integrate key dynamical connections between oceanic flows of distinct scales and dynamics (Naveira Garabato & Meredith, 2022). However, despite the many significant leaps in understanding brought about by technological progress, one important blind spot remains in our ocean observing system: there exists currently no established approach to robustly measure oceanic flows on horizontal scales of O(1–100 m) over any meaningful spatio-temporal domain (e.g., distances of many kilometres, or times of weeks to years). This gap in observational capability has hampered the development of understanding of a breadth of oceanic processes operating on those scales (such as coastal and topographically-pinned boundary jets, submesoscale eddies, and internal waves), and prevented testing of model-based predictions of such processes' dynamics and large-scale impacts (Fox-Kemper et al., 2019).

A potential solution to this observational gap is provided by distributed optical fiber sensing (DOFS), which can enable quasi-continuous information on measurands as a function of distance along the fiber at unprecedentedly high along-fiber (m) and temporal (ms) resolutions over distances of up to tens of kilometres (50 km). The sensing
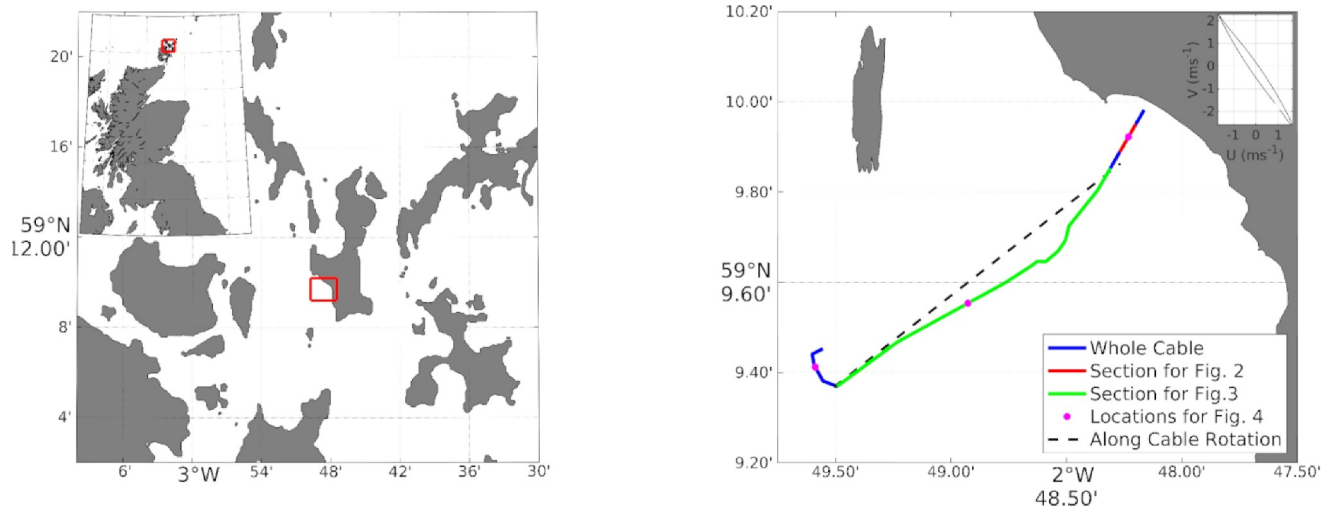
Figure 1. (a) Map of the region, the location of the cable, shown in detail in panel (b), is marked by the red box. (b) The location of the cable is shown in blue. The cable segments used to construct Figures 2 and 3 are respectively marked in red and green. The locations of the wavelet transform analyses in Figure 4 are indicated by magenta circles. The inset in panel (b) is the depth averaged velocity over the observation period.

potential can broadly be split into two components that focus on measuring temperature and strain. These two modes of operation are enabled through the differing sensitivity of the Raman, Brilloun and Rayleigh scatterings to the properties of the fiber. The choice of scattering mechanism used for sensing can be optimized depending on the requirements for measurand(s), cable length, and required resolution. Additionally, the composite construction of the cable the fiber is embedded within can modify how changes in the surrounding environment are communicated to the fiber, for example, by differences in its thermal conductivity or elasticity. This technology is well established in industrial applications (Hartog, 2017), but has only entered environmental science recently—with illustrations of its remarkable potential in the context of marine, terrestrial and glacial geophysics (Becker et al., 2017; Blum et al., 2008; Dou et al., 2017; Hartog et al., 2018; Jousset et al., 2018; Lindsey et al., 2017; Lior et al., 2021; Marra et al., 2018; Sladen et al., 2019; Ugalde et al., 2021; Walter et al., 2020; Wang et al., 2018; Williams et al., 2019; Yu et al., 2019; Zhan, 2019), monitoring of soil moisture (Striegl & Loheide, 2012) and ice-shelf melting (Kobs et al., 2014). In an oceanographic setting, DOFS techniques have shown promise (Lindsey et al., 2019), and are beginning to be applied to measure the near-bottom temperature signatures of internal waves (Lucas & Pinkel, 2022) and for acoustic sensing of surface gravity waves (Williams et al., 2022), using fiber optics within legacy telecommunication cables laid along the seafloor. This technology has many potential applications, encompassing both bespoke deployments and leveraging of the existing vast legacy seafloor infrastructure of telecommunication and energy cables. Here, we expand the scope of these previous studies by demonstrating the capability of DOFS phase-based dynamic differential strain measurements, often called distributed acoustic sensing (DAS), to directly observe near-cable ocean velocity. The technique is grounded on the coherent detection of the phase of the backscattered optical signal (Hartog, 2017), and is applied here to a legacy renewable energy cable.

2. Data and Methods

The Fall of Warness is a 50 m deep channel, located on the south-western coast of Eday, Orkney Islands (Figure 1). The channel runs broadly from north-west to south-east and is characterized by very strong near-rectilinear M2 (12.42 hr) period tides. Due to the intensity of the barotropic tidal currents, which exceed 3 m s^{-1} at spring tide, the area has hosted a European Marine Energy Center (EMEC) tidal energy generation test site. Here we utilize the fiber optic within a legacy power cable linked to this site, in order to demonstrate its ability to record and identify oceanic flow processes in this unusually energetic site.

2.1. Optical Fiber Data

We consider a 12-hr continuous sampling period between 23:34:44 3/11/2020 and 11:41:58 4/11/2020, from cable 4 at the EMEC tidal energy test site. This cable is 108 mm in diameter and runs 2 km from the shore to a test

berth in the thalweg of the channel. The cable is composite comprising three power cores; three 2.5 mm^2 copper cables; and a 12-core optical fiber bundle. The cable is then armored with two layers of galvanized steel wire and a polypropylene outer cover. The cables were initially laid on the sea floor and only intentionally buried from the spring tide low-water mark. The offshore section of the cable sits on rocky terrain with some free spans and rock contacts; however, with reduced impact due to low tension laying of the cable (European Marine Energy Centre, 2015). No turbine was deployed during the collection of the data analyzed here. An opto-electronic interrogation unit (OIU), bespoke-engineered via a well established coherent detection-based dynamic differential strain-sensing (i.e., DAS) technique (Hartog, 2017), enabled remote single-ended interrogation of the fiber optic within the cable. The DAS system used here exploits a multifrequency-probe with heterodyne detection approach (Hartog (2017), Chapter 6.3.5). These features ensure that signal fading is overcome with optimal signal extraction from locations where complete loss of information otherwise may occur due to destructively interfering backscattered signal. The use of heterodyne approach crucially allows for the selection of the intermediate frequency from the receiver output, which is used for phase detection as a function of time (which is then converted to distance along fiber). Mitigation of the COVID-19 pandemic lockdown-related risks motivated engineering of the OIU with remote operability (i.e., off-site access). The cable's fiber optic expression at the power station on land was connected to the OIU by the station's technical personnel, following which the system was operated remotely. Optical pulses of 20 ns were fired over the 2 km length of the cable at a repetition frequency of 1 kHz, for a range of time periods and over several days, with the phase of the backscattered Rayleigh signal coherently recorded. The recorded phase is linearly related to the strain experienced by the cable (Hartog, 2017) under dynamic loading from the ambient physical environment. In the oceanographic setting, this can include local coupling between the water properties and cable as well as acoustic (pressure) waves passing through the cable. These pulses illuminate 2.04 m of cable during propagation, which sets the along-cable spatial resolution of the data. The data stream comprised throughputs at 300 MiB/s, and was subsequently spatially and/or temporally sampled to fit the acquisition requirements around the onboard storage of 3 TB. We present data in three pre-processed formats: full-resolution, filtered at 1 min, and filtered at 1 hr. The filtering was performed using a zero-phase shift first-order low-pass Butterworth filter. Subsequently, the data was separated into 15-min bins for analysis and averaging.

2.2. ADCP Data

A 600 kHz acoustic doppler current profiler (ADCP) mounted in a bottom lander was deployed 740 m to the south of the offshore end of the cable (59° 9.005 N, 2° 49.623 W). This provides conventional oceanographic observations of velocity and bottom pressure every 10 min for a period overlapping with the record of cable measurements. These conventional observations will be used for direct comparison with the cable's phase data.

3. Results

Here we explore the cable data from three perspectives to demonstrate the potential of DOFS to illuminate a wide range of oceanic flow processes. These three perspectives are: nearshore wave breaking; cable-parallel tidal flow; and turbulent-frequency perturbations.

3.1. Nearshore Wave Breaking

The frequency band energy (FBE) expression of the data was calculated along the full cable length. This was done using the traditional approach from signal processing, which entails the computation of the integral of the squared signal magnitude over a time period, within a specific frequency range. The FBE data discussed in this paper were evaluated over 5 s bins within a frequency range of 2–10 Hz. FBE diagnostics enable visualization of the energy dissipated on the cable throughout its length over any temporal interval, whilst keeping the data light-weight. This energy dissipation is due to the dynamic loading effects onto the cable from the diversity of motions in the ambient environment. Consequently, it can inform subsequent analysis that is targeted at specific spatio-temporal regions, in phase space, without having to deal with the entirety of the large data volume at once.

The FBE data reveals enhanced energy in the 2–10 Hz range on a wide range of space-time scales (indicated by the lighter colors in Figure 2a). Patterns of enhanced energy include horizontal bands, which are indicative of cable segments that experience systematically elevated or reduced strain within the 2–10 Hz frequency band throughout the sampling period; and vertical bands, which denote temporal changes in energy at a fixed position
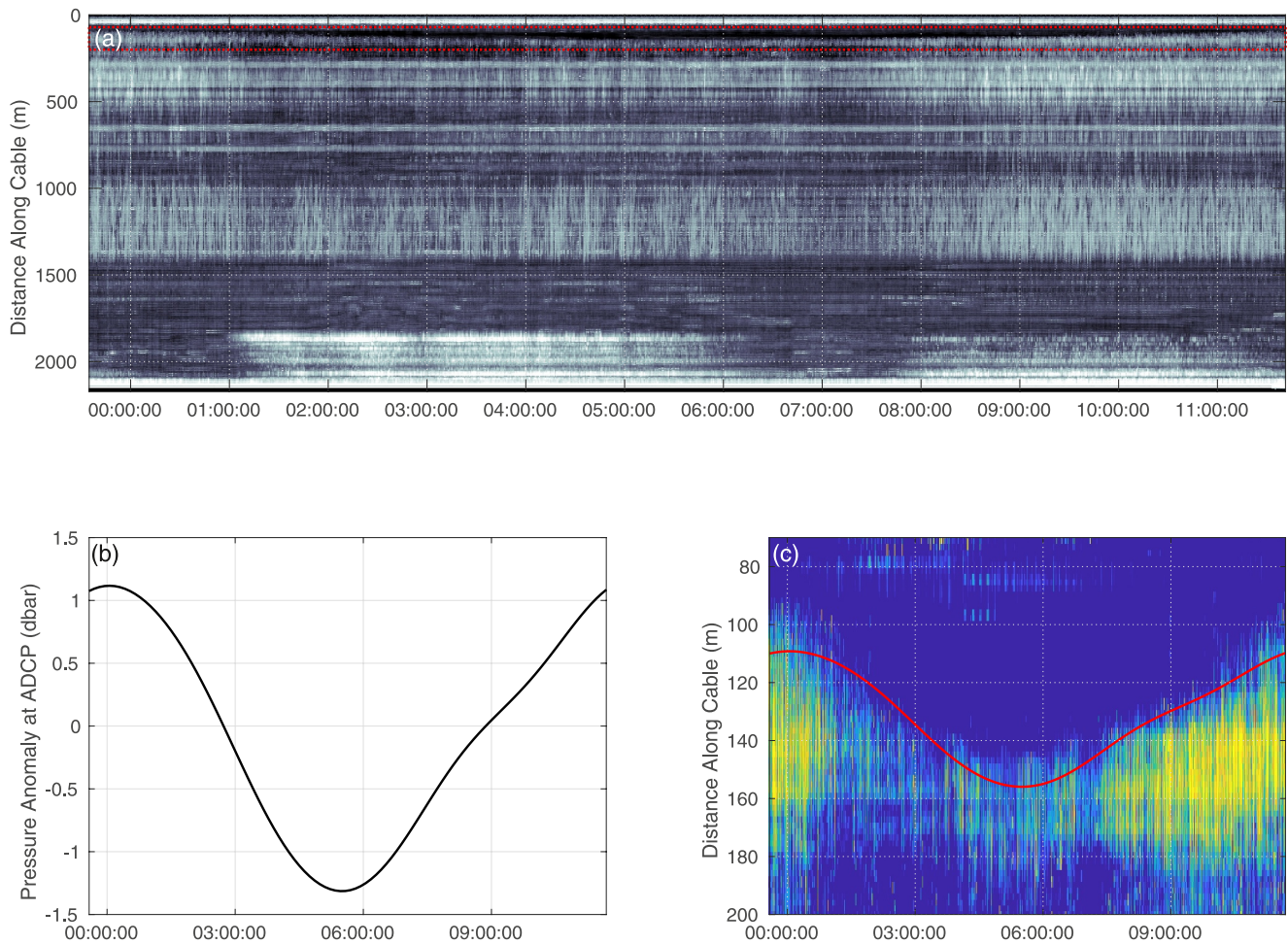
Figure 2. Frequency Band Energy (FBE) data in 5 s bins for 2–10 Hz in time and offshore distance along the cable, for (a) the entire space-time extent with light shades representing enhanced energy, and (c) zoomed on 70–200 m along-cable distance (red box in panel (a) and red line in Figure 1) with yellow shades indicating enhanced energy to highlight nearshore processes. Additionally, (b) the pressure record from the nearby acoustic doppler current profiler is shown. The solid red line in panel (c) is a scaled horizontal excursion using a bottom slope of 0.052.

along the cable. The offshore end of the cable, from 1,800 to 2,100 m, exhibits strong tidal modulation, with enhanced energy from 1:30 to 6 a.m. and after 8:30 a.m. This tidal signal is not symmetric, with the later period showing reduced energy relative to the earlier one. The potential driving mechanisms of these high-frequency signals away from the coast will be discussed in Section 3.3.

The FBE also displays a spatially localized tidal signal at the nearshore end of the cable, whereby a zone of enhanced energy moves offshore from an along-cable distance of 110 m at the start of the time series to 160 m around 6 a.m., and returns to the initial distance from shore by the end. The ADCP bottom pressure record indicates a variation in water depth with the same temporal structure, ranging from a pressure anomaly above the mean of 1.1 dbar (approximately equivalent to a sea level anomaly in meters) at the start and end to −1.3 dbar at the mid-point (Figure 2b). An estimate of the expected horizontal displacement of a certain water depth associated with this change in bottom pressure can be made by scaling the bottom pressure by the topographic slope. The along-cable distance between 6 and 10 m below the mean sea level is 77 m, implying a topographic slope of 0.052. This yields a horizontal displacement of the same magnitude, 46 m, and in phase with the FBE data changes (Figure 2c). We thus surmise that the tidally-modulated translation of the nearshore high-energy zone seen here results from the over-ground movement of coastal wave breaking in response to tidal changes in water depth. Additionally, the reduction in energy around 6 a.m. is likely to reflect the weakening of wave breaking during the tide's ebb phase (low sea level) relative to the flood (high sea level). Such tidal modulation of surface wave height

and energy has been previously identified for macrotidal regimes (Hashemi et al., 2016; Lewis et al., 2014; Wolf, 2009).

3.2. Cable-Parallel Velocity

Next, we will demonstrate the potential of cable strain measurements to act as a proxy for cable-parallel flow. This is mediated through the skin drag on the cable stretching or compressing the cable. An alternative source of very low frequency changes in the measured phase is the thermo-optic effect induced by ocean temperature fluctuations (Quiñones et al., 2023; Williams et al., 2023). In this study the data is from a shallow and strongly tidal channel, resulting in a well mixed water column with weak temperature gradients that could be advected past the cable. As a result, the effects of temperature changes are not considered here.

3.2.1. Theory

The recorded phase (Φ_m) is linearly related to the differential change (Δx) in the length of the illuminated cable section (Hartog, 2017) as,

$$\Phi_m = 4\pi n\xi \frac{\Delta x}{\lambda} + \Phi_b - \Phi_a, \tag{1}$$

where n is the refractive index, ξ is the photoelastic correction factor, λ is the optical wavelength, and Φ_b and Φ_a are the intrinsic phases at either end of the illuminated section. These five are fundamental properties of the optical fiber and are expected to be constant for a given position on the cable, such that temporal changes in the recorded phase are a function of differential length changes. We then assume that the cable has linear elasticity, and rapidly comes to equilibrium with forcing such that the cable length change, Δx, relative to a fixed point is given by Hooke's law,

$$F = k\Delta x, \tag{2}$$

where F is the force acting on the cable, and k is the stiffness of the composite cable. The force driven by the flow acting on the cable can be modeled by the skin drag,

$$F = 0.5\rho u|u|C_d A, \tag{3}$$

where ρ is the water density; u is the cable-parallel velocity; $|u|$ is the cable-parallel speed, such that $u|u|$ is the squared velocity but maintaining the sign (signed square velocity); C_d is the drag coefficient, representative of the roughness of the cable; and A is the area of the cable exposed to the flow from the fixed point to the end of the measurement length used. Combining these gives a linear relation between the signed squared velocity relative to the fixed point and the recorded phase,

$$u|u| = K\Phi_m + C, \tag{4}$$

$$K = \frac{k\lambda}{2\pi n\xi\rho C_d A}, \quad C = \frac{k\lambda(\Phi_a - \Phi_b)}{2\pi n\xi\rho C_d A}, \tag{5}$$

with the coefficients K and C expected to be constant in time, but likely to vary along the cable length and between deployments (depending on the design of the cable, its orientation with respect to local topography, and the nature of the seafloor). The recorded phase from the cable and velocity from the ADCP will now be jointly analyzed in the context of this equation. It is important to note that this equation for the cable strain is built on the assumption that we are measuring the flow relative to a location on the cable that is fixed (either intentionally or by interaction with the seabed). In the case of this study, we are using the whole cable length in the estimates of the flow, with the fixed location being the shore end of the cable.
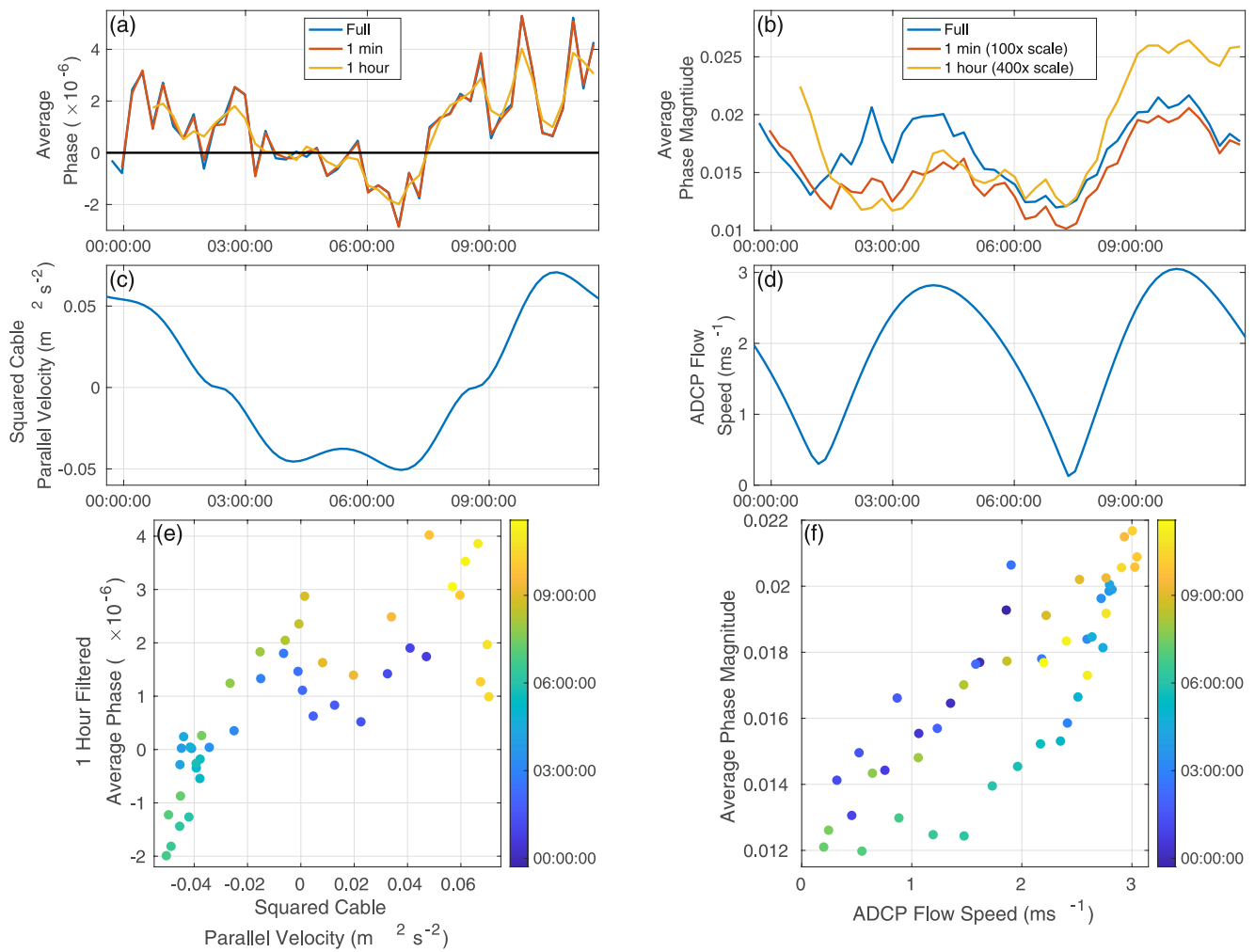
Figure 3. Time-series comparison between cable phase and acoustic doppler current profiler (ADCP) velocity for the 12 hr of observations. The cable phase data is shown averaged in 15-min bins and along the portion of the cable highlighted in Figure 1c. The averages are shown for both the (a) signed and (b) absolute values for unfiltered (blue) and low-pass filtered (at 1 min, red; and at 1 hr, yellow) data. Note that the low-passed data in panel (b) have been multiplied by 100 and 400, respectively. The ADCP velocity is shown as panel (c) signed square in the cable-parallel direction, and (d) full speed past the cable. The two data sets are directly compared in scatter plots of (e) the 1-hr filtered average phase versus the squared cable-parallel velocity, and (f) the unfiltered average phase magnitude versus the flow speed. In both cases. The color of the points indicates the time of measurement.

3.2.2. Observations

Here we present the cable phase data averaged in two ways, in order to compare them with conventional oceanographic observations acquired by the ADCP. First, we will discuss the phase averaged along a section of the cable that excludes the change of direction at its offshore end and the shallow section at the nearshore (green line in Figure 1c). This set of diagnostics is shown in Figures 3a–3c and 3e. Subsequently, in Section 3.3, we will discuss the high-frequency signals in the phase data (Figures 3b–3d and 3f).

The averaged phase is large and positive at the start and end of the time-series, and negative for the central third (Figure 3a). This signal is not sensitive to the choice of filter applied to the phase data (compare the different color lines in Figure 3a), implying that the signal stems primarily from processes occurring with periods greater than 1 hr. There is some additional variability overlaid on the tidal signal, characterized by periods of 1 hr or less that point to the occurrence of higher-frequency or more localized flows around the cable. Given the spatial separation between the cable and the ADCP, we will focus on examining the extent to which the cable phase data reproduces the tidal flow, which is expected to be consistent over horizontal scales larger than the ADCP-cable distance. The signed squared velocity computed from ADCP measurements denotes positive velocities at the start and end of

the time series, indicating stretching of the cable; and negative velocities in the middle of the record, indicating compression (Figure 3c). These ADCP-derived velocities are much weaker (up to 25 cm s^{-1}) than the full tidal flow, as the cable is oriented close to the minor axis of the tide (Figure 1c). Jointly considering the cable phase and ADCP flow data shows an approximately linear relation between the two (Figure 3e). This relation is close to constant in time (see Figure 3e, where colors refer to the time of the observations), and is consistent with Equation 4, with best-fit coefficients of $K = 2.1 \times 10^4$ and $C = -2.2 \times 10^{-2}$ ($R^2 = 0.633$, p value = 1.1×10^{-10}). The variability not captured by this model is primarily associated with the higher-frequency motions super-imposed on the tidal signal, illustrated by R^2 increasing to 0.89 when the data is smoothed using a 6-hr window.

3.3. High-Frequency Signals

Finally, we will explore the relationship between the higher-frequency cable signals and the tidal flow (Figures 3b–3d and 3f). The average of the phase magnitude, taking the absolute value of the phase prior to performing the spatial and temporal averaging, also exhibits a strong tidal modulation. This averaging is indicative of the magnitude of the signal over frequencies spanning from the low-pass filter frequency, 1 kHz for the full data or 1 min/1 hr, to the averaging frequency, 15 min. However, this tidal signal has a different phasing and twice the frequency compared to the tidal signal discussed in the previous section (Figure 3b). The tidally modulated signal in the average phase magnitude has a consistent temporal structure across a range of filters, but the signal's magnitude is highly sensitive to filter choice, with reductions by a factor of 100 and 400 for the 1-min and 1-hr low pass filters, respectively. This implies that, although the signal is present across all frequencies, it is dominated by processes with characteristic periods of less than 1 min. The average phase magnitude signal is in synchrony with the ADCP-measured flow speed, with maxima in the cable signal co-located with the fastest flows (Figure 3d). There is also an asymmetry in the cable's sensitivity to the flow, with the central peak in flow speed (from 2 to 6 a.m.) displaying lower average phase magnitude than the peaks at the start and end of the time series (separation of the light blue points from the dark blue and green/yellow points in Figure 3f). We suggest that this may be due to the way the tidal flow direction interacts with the cable, as the process generating high-frequency motions is likely to be sensitive to the character of the upstream topography.

To further elicit the role of high-frequency motions in governing the cable's response to the tidal flow, we inspect wavelet transforms of the full phase data. Although we computed these for the whole cable, we illustrate key features with three examples, representative of three distinct regimes occurring at different distances along the cable (Figure 1): the first represents the nearshore region discussed in Figure 2; the second represents the middle of the cable; and the third represents a position near the end of the cable, where the cable has changed direction relative to the flow. All three of the wavelets are dominated by high-frequency energy, in the range of 0.2–10 Hz (Figures 4a–4c and 4e). At the nearshore location, the magnitude of this dominant high-frequency signal is consistent with the tidal spatial migration of coastal wave breaking seen in Section 3.1 (Figure 4a). Such structure is primarily seen at high frequencies, with lower frequencies (<0.1 Hz) displaying little or no signal of tidal modulation (Figure 4b). This is consistent with the tidal modulation having a low-frequency limit set by the surface peak wave period, typically 10 s at this site (Sellar et al., 2018). At the mid-cable wavelet, we again observe dominance of high frequencies, but with limited tidal modulation of those signals (Figure 4c). The scaled wavelet indicates that this lack of tidal modulation applies across all frequencies (Figure 4d). There is, however, modulation on periods less than 1 hr indicated by the vertical stripes. The offshore end of the cable displays strong tidal modulation (at half the M2 period) of the high-frequency signal, which once again is dominated by frequencies higher than 1 Hz (Figure 4e). In this case, in contrast to the nearshore regime, the tidal modulation extends onto much lower frequencies, reaching periods of 5 min (Figure 4f). This implies that a comparatively low-frequency process is driving variability in this region with the signal cascading to higher frequencies, consistent with a control by tidal speed.

The dominant frequencies in the wavelets are potentially compatible with a range of turbulent processes. The first is the natural turbulence generated by the tidal flow's interaction with the ocean bottom. In this case, the relevant frequency scales are those associated with the inertial subrange of three-dimensional turbulence, with Ozmidov scales representing the most energetic (Tennekes & Lumley, 1972). For a fast-flowing, weakly stratified channel, the Ozmidov scale is typically 1–10 m (Stevens, 2018); if we invoke the frozen-field hypothesis (Taylor, 1938) and a flow speed of 2 m s^{-1}, the expected frequency of the turbulence would be 0.2–2 Hz, in line with our observations. The alternative interpretation would be that the motions are generated by vortex-induced vibrations (VIVs) driven by the impingement of the flow on the cable. VIV is only possible when the cable is decoupled from
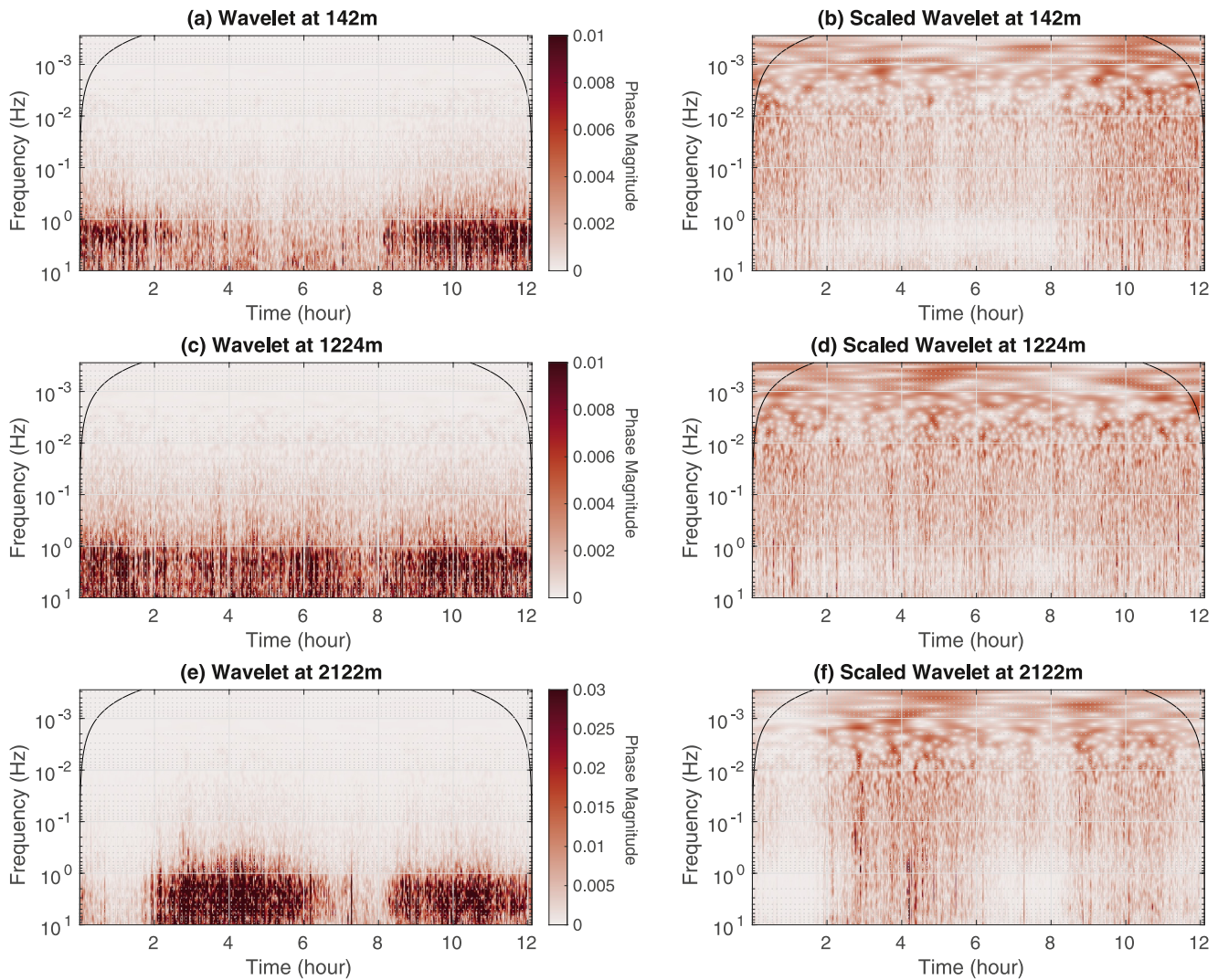
Figure 4. Continuous wavelet transform magnitude of the cable phase data at three locations: (a, b) 142 m; (c, d) 1,224 m; and (e, f) 2,122 m from the nearshore end. The wavelet transform is shown in panels (a, c, e), and the wavelet scaled by the standard deviation for each frequency is shown in panels (b, d, f).

the seabed, for example, spanning between two points. This scenario is likely to occur only for parts of the cable. The relevant scale for VIVs is the Strouhal frequency (Fey et al., 1998). Taking a typical Strouhal number of 0.2, a flow speed of 2 m s^{-1}, and a cable diameter of 0.1 m gives a Strouhal frequency of 4 Hz again within the frequency range of our observed signals. A final potential source of signals in this frequency range is the generation of acoustic and seismic waves by wave breaking in the surf zone (Garcés et al., 2003; Poppeliers & Mallinson, 2015). This process is potentially important in the wavelet presented close to the shore (Figure 4a), where the phasing of the high-frequency signal is aligned with the changes in the magnitude of the wave breaking signal seen in Figure 2, that is, high at the start and end of the time series and suppressed in the middle. For the offshore wavelets the timing of the signal is rather different, supporting the other interpretations presented above. The separation and interpretation of these processes is complex, and will be the subject of future work.

4. Summary and Outlook

In this paper, we provide an initial demonstration of how optical fibers within legacy seafloor cables can be used as distributed remote passive sensing arrays that are sensitive to a range of oceanic flow phenomena. We utilize a 12-hr time series of distributed fiber-optic dynamic differential strain data from a legacy energy cable to identify several flow processes. First, we document wave breaking at the coastal end of the cable, and detect the changes in

the location and intensity of breaking through a tidal cycle. Second, we examine the dynamic load due to stretching/compression-driven tidal flows in the cable-parallel direction, using low-frequency differential strain changes. These are quantified using the linearly varying differential changes in the phase of the backscattered optical signal under such loading effects. Finally, we observe high-frequency dynamic differential strain signals linked to the tidal flow speed, primarily in the cable-normal direction. We argue that these signals likely result from processes controlled by the interaction of the tidal flow with either the ocean bottom generating turbulence or the cable body generating vortices. This suite of cable observations are corroborated by a nearby ADCP, which provides velocity and bottom pressure information that is consistent with the cable measurements. Whilst the flows explored in this study are unusually strong, a similar approach could be taken in other regions with more typical oceanographic flows. In these cases, further analysis of the sensitivity of the method and adjustments to increase the sensitivity, for example, by increasing the skin drag or reducing the stiffness of the cable, would be valuable.

The exploitation of fiber optics within legacy seafloor cables as remote passive ocean velocity sensors, demonstrated here for a strong flow, represents a potentially significant advance in the observation of oceanic flows beyond the traditional approaches that only provide data at one location for in situ observations or only the barotropic component for satellite altimetry. This is especially so in view of the potential for low-cost, sustainable, wide-area coverage and its filling of the crucial blind spots on horizontal scales of $O(1-100\ \mathrm{m})$ that currently hampers the ocean observing system. This is enabled by the single-ended, on-land interrogation of cables, requiring no additional deployment at sea alongside the potential for real-time data availability for immediate analysis and interpretation, in contrast to other approaches that typically only provide data on instrument recovery. There is a significant legacy seafloor cable infrastructure of telecommunication cables, over 1 million km across more than 500 cables, that can be utilized to make observations of this type. These cables, however, are not equally distributed across the global ocean, with good cross-basin coverage in the North Atlantic and North Pacific and following coastlines, but more limited cross-basin coverage in the southern hemisphere including no legacy cables in the Southern Ocean. The approach described here also lays the ground for bespoke deployments of fiber optic cables—both in the horizontal and vertical, and on a range of platforms—targeting specific oceanic flow processes. However, further work is required to fully realise the oceanographic potential of DOFS. For example, while the association between the differential change in phase of the backscattered optical signal with the along-cable strain is well understood, the relationship between the strain and the dynamic properties of the surrounding oceanic environment is less conclusive. This limitation results in uncertainties in for example, the applicability of the assumptions underpinning Equation 4, the stability of the derived coefficients, and the optimal conventional measurements required to calibrate those parameters. This work constitutes an initial assessment of the above relationship, and motivates a dedicated observational campaign to rigorously and comprehensively characterize the DOFS methodology presented here for a wider range of oceanic environments.

Data Availability Statement

The data files used in this paper are available at (Spingys et al., 2023).

References

Becker, M. W., Ciervo, C., Cole, M., Coleman, T., & Mondanos, M. (2017). Fracture hydromechanical response measured by fiber optic distributed acoustic sensing at milliHertz frequencies: Fracture Hydromechanics from DAS. *Geophysical Research Letters*, *44*(14), 7295–7302. https://doi.org/10.1002/2017GL073931

Blum, J. A., Nooner, S. L., & Zumberge, M. A. (2008). Recording Earth strain with optical fibers. *IEEE Sensors Journal*, *8*(7), 1152–1160. https://doi.org/10.1109/JSEN.2008.926882

Davis, R. E., Talley, L. D., Roemmich, D., Owens, W. B., Rudnick, D. L., Toole, J., et al. (2019). 100 years of progress in ocean observing systems. *Meteorological Monographs*, *59*(1), 3.1–3.46. https://doi.org/10.1175/AMSMONOGRAPHS-D-18-0014.1

Dou, S., Lindsey, N., Wagner, A. M., Daley, T. M., Freifeld, B., Robertson, M., et al. (2017). Distributed acoustic sensing for seismic monitoring of the near surface: A traffic-noise interferometry case study. *Scientific Reports*, *7*(1), 11620. https://doi.org/10.1038/s41598-017-11986-4

European Marine Energy Centre. (2015). PFOW enabling actions project: Sub-sea cable lifecycle study.

Fey, U., König, M., & Eckelmann, H. (1998). A new Strouhal–Reynolds-number relationship for the circular cylinder in the range 47. *Physics of Fluids*, *10*(7), 1547–1549. https://doi.org/10.1063/1.869675

Fox-Kemper, B., Adcroft, A., Böning, C. W., Chassignet, E. P., Curchitser, E., Danabasoglu, G., et al. (2019). Challenges and prospects in ocean circulation models. *Frontiers in Marine Science*, *6*. https://doi.org/10.3389/fmars.2019.00065

Garcés, M., Hetzer, C., Merrifield, M., Willis, M., & Aucan, J. (2003). Observations of surf infrasound in Hawai'i. *Geophysical Research Letters*, *30*(24). https://doi.org/10.1029/2003GL018614

Hartog, A. H. (2017). *An introduction to distributed optical fibre sensors*. CRC Press. https://doi.org/10.1201/9781315119014

Hartog, A. H., Belal, M., & Clare, M. A. (2018). Advances in distributed fiber-optic sensing for monitoring marine infrastructure, measuring the deep ocean, and quantifying the risks posed by seafloor Hazards. *Marine Technology Society Journal*, *52*(5), 58–73. https://doi.org/10.4031/MTSJ.52.5.7

Hashemi, M. R., Grilli, S. T., & Neill, S. P. (2016). A simplified method to estimate tidal current effects on the ocean wave power resource. *Renewable Energy*, *96*, 257–269. https://doi.org/10.1016/j.renene.2016.04.073

Jousset, P., Reinsch, T., Ryberg, T., Blanck, H., Clarke, A., Aghayev, R., et al. (2018). Dynamic strain determination using fibre-optic cables allows imaging of seismological and structural features. *Nature Communications*, *9*(1), 2509. https://doi.org/10.1038/s41467-018-04860-y

Kobs, S., Holland, D. M., Zagorodnov, V., Stern, A., & Tyler, S. W. (2014). Novel monitoring of Antarctic ice shelf basal melting using a fiber-optic distributed temperature sensing mooring. *Geophysical Research Letters*, *41*(19), 6779–6786. https://doi.org/10.1002/2014GL061155

Lewis, M. J., Neill, S. P., Hashemi, M. R., & Reza, M. (2014). Realistic wave conditions and their influence on quantifying the tidal stream energy resource. *Applied Energy*, *136*, 495–508. https://doi.org/10.1016/j.apenergy.2014.09.061

Lindsey, N. J., Dawe, T. C., & Ajo-Franklin, J. B. (2019). Illuminating seafloor faults and ocean dynamics with dark fiber distributed acoustic sensing. *Science*, *366*(6469), 1103–1107. https://doi.org/10.1126/science.aay5881

Lindsey, N. J., Martin, E. R., Dreger, D. S., Freifeld, B., Cole, S., James, S. R., et al. (2017). Fiber-optic network observations of earthquake wavefields. *Geophysical Research Letters*, *44*(23), 11792–11799. https://doi.org/10.1002/2017GL075722

Lior, I., Sladen, A., Rivet, D., Ampuero, J.-P., Hello, Y., Becerril, C., et al. (2021). On the detection capabilities of underwater distributed acoustic sensing. *Journal of Geophysical Research: Solid Earth*, *126*(3), e2020JB020925. https://doi.org/10.1029/2020JB020925

Lucas, A. J., & Pinkel, R. (2022). Observations of coherent transverse wakes in shoaling nonlinear internal waves. *Journal of Physical Oceanography*, *52*(6), 1277–1293. https://doi.org/10.1175/JPO-D-21-0059.1

Marra, G., Clivati, C., Luckett, R., Tampellini, A., Kronjäger, J., Wright, L., et al. (2018). Ultrastable laser interferometry for earthquake detection with terrestrial and submarine cables. *Science*, *361*(6401), 486–490. https://doi.org/10.1126/science.aat4458

Naveira Garabato, A., & Meredith, M. (2022). Chapter 1 - Ocean mixing: Oceanography at a watershed. In M. Meredith & A. Naveira Garabato (Eds.), *Ocean mixing* (pp. 1–4). Elsevier. https://doi.org/10.1016/B978-0-12-821512-8.00008-6

Poppeliers, C., & Mallinson, D. (2015). High-frequency seismic noise generated from breaking shallow water ocean waves and the link to time-variable sea states. *Geophysical Research Letters*, *42*(20), 8563–8569. https://doi.org/10.1001/2015GL066126

Quiñones, J. D. P., Sladen, A., Ponte, A., Lior, I., Ampuero, J.-P., Rivet, D., et al. (2023). High resolution seafloor thermometry for internal wave and upwelling monitoring using distributed acoustic sensing. *Scientific Reports*, *13*(1), 17459. https://doi.org/10.1038/s41598-023-44635-0

Sellar, B., Wakelam, G., Sutherland, D., Ingram, D., & Venugopal, V. (2018). Characterisation of tidal flows at the European marine energy Centre in the absence of ocean waves. *Energies*, *11*(1), 176. https://doi.org/10.3390/en11010176

Sladen, A., Rivet, D., Ampuero, J. P., De Barros, L., Hello, Y., Calbris, G., & Lamare, P. (2019). Distributed sensing of earthquakes and ocean-solid Earth interactions on seafloor telecom cables. *Nature Communications*, *10*(1), 5777. https://doi.org/10.1038/s41467-019-13793-z

Spingys, C., Garabato, A. N., & Belal, M. (2023). Distributed fibre optic sensing for high space-time resolution ocean velocity observations: A case study from a macrotidal channel [Dataset]. *Zenodo*. https://doi.org/10.5281/zenodo.7896794

Stevens, C. L. (2018). Turbulent length scales in a fast-flowing, weakly stratified, strait: Cook Strait, New Zealand. *Ocean Science*, *14*(4), 801–812. https://doi.org/10.5194/os-14-801-2018

Striegl, A. M., & Loheide, S. P., II. (2012). Heated distributed temperature sensing for field scale soil moisture monitoring. *Ground Water*, *50*(3), 340–347. https://doi.org/10.1111/j.1745-6584.2012.00928.x

Taylor, G. I. (1938). The spectrum of turbulence. *Proceedings of the Royal Society of London. Series A - Mathematical and Physical Sciences*, *164*(919), 476–490. https://doi.org/10.1098/rspa.1938.0032

Tennekes, H., & Lumley, J. L. (1972). *A first course in turbulence*. MIT Press.

Ugalde, A., Becerril, C., Villaseñor, A., Ranero, C. R., Fernández-Ruiz, M. R., Martin-Lopez, S., et al. (2021). Noise levels and signals observed on submarine fibers in the Canary Islands using DAS. *Seismological Research Letters*, *93*(1), 351–363. https://doi.org/10.1785/0220210049

Walter, F., Gräff, D., Lindner, F., Paitz, P., Köpfli, M., Chmiel, M., & Fichtner, A. (2020). Distributed acoustic sensing of microseismic sources and wave propagation in glaciated terrain. *Nature Communications*, *11*(1), 2436. https://doi.org/10.1038/s41467-020-15824-6

Wang, H. F., Zeng, X., Miller, D. E., Fratta, D., Feigl, K. L., Thurber, C. H., & Mellors, R. J. (2018). Ground motion response to an ML 4.3 earthquake using co-located distributed acoustic sensing and seismometer arrays. *Geophysical Journal International*, *213*(3), 2020–2036. https://doi.org/10.1093/gji/ggy102

Williams, E. F., Fernández-Ruiz, M. R., Magalhaes, R., Vanthillo, R., Zhan, Z., González-Herráez, M., & Martins, H. F. (2019). Distributed sensing of microseisms and teleseisms with submarine dark fibers. *Nature Communications*, *10*(1), 5778. https://doi.org/10.1038/s41467-019-13262-7

Williams, E. F., Ugalde, A., Martins, H. F., Becerril, C. E., Callies, J., Claret, M., et al. (2023). Fiber-optic observations of internal waves and tides. *Journal of Geophysical Research: Oceans*, *128*(9). https://doi.org/10.1029/2023JC019980

Williams, E. F., Zhan, Z., Martins, H. F., Fernández-Ruiz, M. R., Martín-López, S., González-Herráez, M., & Callies, J. (2022). Surface gravity wave interferometry and ocean current monitoring with ocean-bottom DAS. *Journal of Geophysical Research: Oceans*, *127*(5), e2021JC018375. https://doi.org/10.1029/2021JC018375

Wolf, J. (2009). Coastal flooding: Impacts of coupled wave–surge–tide models. *Natural Hazards*, *49*(2), 241–260. https://doi.org/10.1007/s11069-008-9316-5

Yu, C., Zhan, Z., Lindsey, N. J., Ajo-Franklin, J. B., & Robertson, M. (2019). The potential of DAS in Teleseismic studies: Insights from the goldstone experiment. *Geophysical Research Letters*, *46*(3), 1320–1328. https://doi.org/10.1029/2018GL081195

Zhan, Z. (2019). Distributed acoustic sensing turns fiber-optic cables into sensitive seismic antennas. *Seismological Research Letters*, *91*(1), 1–15. https://doi.org/10.1785/0220190112